



# Validation and uncertainty quantification of detector response functions for a 1"×2" NaI collimated detector intended for inverse radioisotope source mapping applications



N. Nelson<sup>a,\*</sup>, Y. Azmy<sup>a</sup>, R.P. Gardner<sup>a</sup>, J. Mattingly<sup>a</sup>, R. Smith<sup>b</sup>, L.G. Worrall<sup>c</sup>, S. Dewji<sup>c</sup>

<sup>a</sup> Dept. of Nuclear Engineering, NC State University, 2500 Stinson Drive, 3140 Burlington Engineering Labs, Raleigh, NC, United States

<sup>b</sup> Dept. of Mathematics, Box 8205, NC State University, Raleigh, NC, United States

<sup>c</sup> Oak Ridge National Laboratory, P.O. Box 2008, Oak Ridge, TN, United States

## ARTICLE INFO

### Article history:

Received 3 March 2017

Received in revised form 16 July 2017

Accepted 18 July 2017

Available online 5 August 2017

### Keywords:

NaI collimated detector

Response function

Validation

Uncertainty quantification

Holdup measurements

## ABSTRACT

Detector response functions (DRFs) are often used for inverse analysis. We compute the DRF of a sodium iodide (NaI) nuclear material holdup field detector using the code named g03 developed by the Center for Engineering Applications of Radioisotopes (CEAR) at NC State University. Three measurement campaigns were performed in order to validate the DRF's constructed by g03: on-axis detection of calibration sources, off-axis measurements of a highly enriched uranium (HEU) disk, and on-axis measurements of the HEU disk with steel plates inserted between the source and the detector to provide attenuation. Furthermore, this work quantifies the uncertainty of the Monte Carlo simulations used in and with g03, as well as the uncertainties associated with each semi-empirical model employed in the full DRF representation. Overall, for the calibration source measurements, the response computed by the DRF for the prediction of the full-energy peak region of responses was good, i.e. within two standard deviations of the experimental response. In contrast, the DRF tended to overestimate the Compton continuum by about 45–65% due to inadequate tuning of the electron range multiplier fit variable that empirically represents physics associated with electron transport that is not modeled explicitly in g03. For the HEU disk measurements, computed DRF responses tended to significantly underestimate (more than 20%) the secondary full-energy peaks (any peak of lower energy than the highest-energy peak computed) due to scattering in the detector collimator and aluminum can, which is not included in the g03 model. We ran a sufficiently large number of histories to ensure for all of the Monte Carlo simulations that the statistical uncertainties were lower than their experimental counterpart's Poisson uncertainties. The uncertainties associated with least-squares fits to the experimental data tended to have parameter relative standard deviations lower than the peak channel relative standard deviation in most cases and good reduced chi-square values. The highest sources of uncertainty were identified as the energy calibration polynomial factor (due to limited source availability and NaI resolution) and the Ba-133 peak fit (only a very weak source was available), which were 20% and 10%, respectively.

© 2017 Published by Elsevier B.V.

## 1. Introduction

A detector response function (DRF) is a function that converts the energy-dependent flux of incoming source particles incident on a detector into a detector response (pulse height) spectrum corresponding to that observed in experimental detector measurements. The DRF is used to characterize an unknown source distribution as in the problem of nuclear material controls and accountancy in quantifying Material Unaccounted For in the form

of holdup [1], the target application of this work. DRFs have been investigated and developed for several research and industrial detection applications. These applications include neutron depth profiling in substrate manufacturing [2], cosmic radiation detection and atmospheric monitoring [3], and positron emission tomography [4]. DRFs have been proposed for nuclear safeguards and security applications as well, such as border monitoring for illegal transport of radioactive materials, cargo and package monitoring, and unknown source identification at source recovery sites.

At present, neither a rigorous mathematical formulation nor a complete physical model exists to describe DRFs. Instead, several stochastic (Monte Carlo) and empirical models are available and

\* Corresponding author.

E-mail address: [nnelson@ncsu.edu](mailto:nnelson@ncsu.edu) (N. Nelson).

reported in the literature. Gardner developed a DRF model through empirical curve fitting and Monte Carlo analysis [5]. He validated his DRF against high-fidelity experimental measurements reported by Heath [6] for 3"×3" and 6"×6" bare NaI detectors using Cs-137 sources centered on the detector's front axis at a distance of 10 cm. There was agreement between Gardner's DRF-computed responses and Heath's benchmark detector measurements of the same detector sizes within two standard deviations of the measured Poisson uncertainty. Gardner's model was also found to be more efficient (required far fewer particle histories for comparatively accurate calculation) and was shown to match better with the Heath experiments than MCNP's F8 pulse-height tally.

In this work the NaI DRF model developed by Gardner is used to characterize a NaI 1"×2" detector for on-axis, off-axis, and attenuated configurations and to validate it against experimental measurements using Cs and HEU sources. Also, uncertainty in the model is calculated by both Frequentist and Bayesian methods and compared to measurement and Monte Carlo transport uncertainties.

### 1.1. Detector response functions

Mathematically, the DRF, denoted  $R(H, E)$ , is defined as the probability that a photon incident on the detector with energy  $E$  yields a pulse with height  $H$  [7]. We employ Gardner's DRF model in our work due to its efficiency and also because MCNP simulates responses according to direct energy deposition in the detector crystal without generating a DRF. A DRF comprises a matrix whose rows represent the energy of an incident photon and columns correspond to detector channels. Elements of the matrix indicate the probability of producing a pulse in a channel due to an incident photon with the given energy. DRFs have been employed in various applications and more recently have gained interest for use in inverse transport problems. An accurate DRF matrix equipped with uncertainty estimates is essential for the success of these applications. The reason for this is the fact that inverse problems seeking the determination of a radiation source distribution from a set of measured detector responses typically require repeated evaluation of modeled detector responses in the process of searching the state space for an optimal inverse solution. For computationally intensive models like radiation transport, repeating such forward computations for each evaluated state would be prohibitively expensive. Instead, computing the adjoint flux (particle importance) for the same configuration using the column sum of the detector's response function matrix as the adjoint source vector provides an inexpensive means to evaluate the response as the inner product of the resulting adjoint flux with the source distribution characterizing the tested state. Consequently, more states can be tested in search for the distribution that best fits the measured responses, thus improving the quality of the solution to the inverse problem.

Gardner's model generates a DRF for a desired detector size, source distance and source energy (single peak), and it accounts for the nonlinear dependence of NaI scintillation efficiency  $\left(\frac{\text{scintillation light yield}}{\text{energy deposited}}\right)$  [%] on the energy deposited in the detector by the incident photon through the following steps [5]. First, a Monte Carlo calculation is conducted with the DRFNCS code [8] to simulate several hundred detector response spectra where photons interactions are only allowed to occur within the detector cell (forced collisions), but leakage of secondary particles is allowed, producing the continuum segment of the spectra. Only about 100,000 particle histories are necessary to produce results with uncertainty under 1%, whereas MCNP F8 Gaussian energy-broadened (GEB) spectra require at least 100 times as many histories to post-process the Gaussian spectral peaks.

Next, the peaks are stripped from the response spectra so that each continuum can be processed separately. Principal component analysis (PCA) is then performed on the correlated response variables and the covariance matrix to produce a small set of uncorrelated variables (principal components). The principal components and the mean vector are stored as data that reproduces an accurate continuum when multiplied with the desired number of channels. Essentially, the continuum can be constructed efficiently without the need for repeated Monte Carlo simulations for each DRF generated.

So, when a new DRF is to be generated, the algorithm need only to generate the full-energy peak of interest by Monte Carlo transport simulation and adds this contribution to the archived continuum to produce the desired DRF [8]. The modified version of DRFNCS (adjusted by the nonlinear scintillation efficiency) is implemented in the computer code g03.

Finally, the Monte Carlo simulation in g03 is modified by several empirical equations to correct pieces of the spectra that are not simulated fully by the Monte Carlo calculation. The g03 DRF peak section is spread according to the power law based on Gaussian peak fitting of measured detector response spectra

$$\sigma_T(E_I) = aE_I^b, \quad (1)$$

where  $a$  and  $b$  are empirical fit parameters, and  $E_I$  is the energy of the incident photon.  $\sigma_T(E_I)$  is the Gaussian uncertainty of the measured full-energy peak. Equation (1) is a semi-empirical model representing the Gaussian peak response spread, whose parameters are found by the least-squares fitting of standard deviations of experimentally measured full-energy peak responses produced by the detector of interest [5].

The flat Compton continuum of the DRF is computed by various empirical fits of the entire experimental responses (not only the peaks). This is necessary because there is as of yet some unmodeled phenomena causing a higher magnitude of the simulated continuum than predicted by the included physics models and observed in the measured data. Simple Compton scattering and partial energy deposition physics due to electron or photon leakage through the detector walls can predict the general flat shape of the Compton continuum but underestimate its magnitude. A normalization factor was developed to account for this effect called the electron range multiplier, since the effect causing the underestimation of the continuum was believed to be connected to the electron range in crystalline materials [9]. The empirical relation is given by

$$R_e = 1 + A_1 e^{(-A_2 E_I)} + A_3 e^{(-A_4 E_I)} \quad (2)$$

$$A_1 = 39.662, \quad A_2 = 3.4052, \quad A_3 = 1.5434, \quad A_4 = 0.1576,$$

where  $E_I$  is again the energy of the incident photon, and  $A_1$  through  $A_4$  are fit parameters determined from experimental responses. This unitless factor ( $R_e$ ) is a pseudo-electron range factor designed to correct the magnitude of the synthetic Compton continuum produced by Gardner's DRF. It was originally fit through trial and error for uncollimated 3"×3" NaI detectors [9] and therefore may be a source of additional error for the 1"×2" NaI detector of interest in this work.

### 1.2. Uncertainty quantification

In the process of comparing measured to computational model results there is measurement uncertainty, model uncertainty, and numerical (simulation) uncertainty. Radiation counting (measurement) and Monte Carlo sampling uncertainty approximately follow a Poisson distribution [10,11].

Determination of the model parameter uncertainty is a more difficult task. Since the core of Frequentist Theory requires a large

number of data points, a Bayesian method was preferred for determining the uncertainty in the Gaussian standard deviation parameter,  $\sigma_T(E_i)$ , of the fit of the spectral response peaks that are needed for the power law fit, Eq. (1). Bayesian methods were also used for determining the parameter uncertainties in the power law itself, and the energy calibration fit. Whereas Frequentist methods were chosen for parameter uncertainty quantification of the computed Gaussian fits for shifting spectra, Gaussian fits of the peaks of experimental spectra were used for the energy calibration due to the abundance of channels in the peaks of those spectra and for efficient calculation [12].

## 2. Experimental setup

The experimental measurement campaign was performed at Oak Ridge National Laboratory (ORNL). The detector of interest for validation of Gardner's DRF model is a 1 in. diameter by 2 in. tall right cylinder EFC Model 1X2P collimated NaI detector. This small detector is used in uranium holdup experiments at ORNL and is an example of a detector used for field measurements of holdup within the Holdup Measurement System (HMS) [13]. The detector is well shielded with lead except on the front face where the collimator aperture allows radiation into the detector from a limited extent of directions, i.e. fixed solid angle. Hence, the detector has approximately a 23 degree field of view, i.e. in-axial-plane angle of vision from the axis normal to its circular front. The rest of the detector components are fairly standard.

Overall, measurements were taken far from the room's walls, with the source and the detector placed on a laboratory bench with an aluminum tee in the setup. It was assumed that scattering off the table and floor would be insignificant since they are low-Z materials and have small scattering cross sections. Scattering off the Al tee was also assumed to be negligible. Therefore, the room geometry and the aluminum tee were not simulated in the Monte Carlo Model described in the next section.

The parameters of all of the sources used for the validation measurements (excluding the reference sources, i.e., Am-241, Ba-133, Mn-54, and Na-22) described in this section are listed in Table 1. The activities of the reference sources used for characterizing the basic detector properties (i.e., energy calibration and the power law fit from peak resolution) are not reported here, as these measurements only required energy and peak response information.

Note that only the active volume of these sources was simulated in MCNP and not the plastic case surrounding them, since attenuation in the casing was assumed to be negligible. The emission energies and relative intensities of the gamma rays of interest for each source (including the detector seed source Am-241 and the reference sources: Ba-133, Mn-54, and Na-22) are listed in Table 2.

In the first set of experiments, a source was placed at a set distance from the detector center (on-axis). The source was held in place on a ring stand, or taped to the front of the detector for quick counts. In this first set of experiments the source was a button calibration source with known activity and dimensions.

**Table 2**

Gamma-ray energies and yields, with uncertainty in parentheses, of all deployed sources were taken from Brookhaven National Laboratory's Nudat2.6 database [16]. Unlisted uncertainties were assumed to be one in the last digit.

Source	Peak No.	Energy (keV)	Yield (%)
Am-241	1	59.5409(1)	35.9(4)
U-235	1	105.0(1)	2.00(3)*
U-235	2	109.0(1)	2.16(13)*
U-235	3	143.76(2)	10.96(14)
U-235	4	163.356(3)	5.08(6)
U-235	5	185.715(5)	57.0(6)
U-235	6	202.12(1)	1.080(23)
U-235	7	205.316(10)	5.02(6)
Ba-133	1	80.9979(11)	35.6(3)*
Ba-133	2	356.0129(7)	62.05(1)
Cs-137	1	661.657(3)	85.10(20)
Mn-54	1	834.848(3)	99.9760(10)
Na-22	1	1274.537(7)	99.941(14)
Co-60	1	1173.228(3)	99.85(3)
Co-60	2	1332.492(4)	99.9825(6)

\* Note: gamma rays from the same source that were within 1 keV of each other were averaged and their intensities summed together.

The next set of experiments focused on the source of primary interest in our work that ultimately targets holdup applications (U-235) and were specifically conducted for the DRF validation exercise. Since it is very unlikely that a detector will be directly pointed at a holdup material deposit when the deposit has an unknown location, strength, and shape, off-axis detector spectra are of great interest in the holdup application. This is also necessary for holdup configurations where the source is spatially distributed and thus contributes to the response of a stationary detector from a broad range of angles of incidence. So, a source was affixed to an aluminum tee and prepared specifically for accurate off-axis measurements.

The detector was placed on the center steel bar while the source was put on the crossbar held by a vice and a steel ring holder at a distance of 38 cm from the detector face (41 cm from the front face of the detector crystal). The source was then moved laterally left and right of center, or the axially aligned position, in 5 cm intervals up to 20 cm in each direction. Measurements ceased at 20 cm because the source started to become indistinguishable from background beyond that distance. For visual reference, the lateral off-axis experimental setup is shown in Fig. 1.

The source was an HEU disk source of known activity, dimensions (reported in Table 1), and enrichment. The source in the disk is composed of uranium metal with traces of carbon. The uranium compound is set on polyethylene epoxy and encased in stainless steel. The activity of the disk was 23.5  $\mu$ Ci on December 1, 2004. However, since U-235 has a very long half-life (703.8 million years), the activity of the source at the time of the measurement is well approximated by its initial activity. The individual uranium nuclides that comprise the disk source employed in our experimental campaign are listed in Table 3.

U-235 is a common special nuclear material of concern to many radiation source detection problems. In unknown source characterization, the isotope of interest, namely, U-235, is detected and

**Table 1**

Dimensions and activities of the sources used for experimental measurements.

Source	A.R. (cm)	Thick. (cm)	Act. ( $\mu$ Ci)	Created	Measured	Calc. Act. ( $\mu$ Ci)
Cs-137*	0.25	0.318	5.01	9/28/2005	2/20/2014	4.13 $\pm$ 15%
Co-60*	0.25	0.318	0.8516	3/1/2002	6/21/2013	0.1927 $\pm$ 15%
U Disk	2.381	0.0701	23.5	12/5/2004	2/20/2014	23.5 $\pm$ 10%

\* Note: All calibration sources used in this work were created by Eckert and Ziegler, and the active source dimensions (active radius, A.R., and thickness) used in the MCNP model were taken from the Type D disk model in the catalog. Furthermore, according to the supplier, "Sources are manufactured with contained activity (Act.) values of  $\pm$ 15% of the requested activity value unless otherwise noted in the catalog" [15].

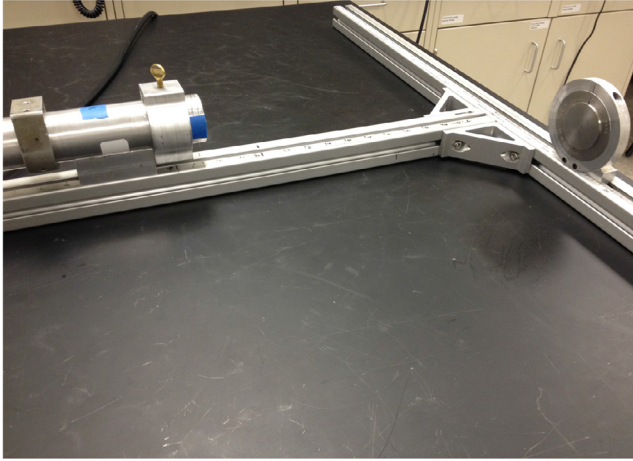


**Fig. 1.** The HEU disk off-axis experiment 41 cm from the front face of the detector crystal and 15 cm to the right ( $x = +15$  cm).

**Table 3**  
Isotopic composition of the uranium disk source.

Nuclide	Weight %
U-234	1.016
U-235	93.162
U-236	0.400
U-238	5.421
C (natural)	1.009E-3

quantified on the basis of its gamma-ray emissions. Hence, the focus of the validation experiments has been on the low energies of the detector spectrum where the highest intensity (most probable) gamma rays of U-235 are emitted (140–190 keV). This also explains the choice of a smaller NaI detector size, as high-energy detection that would necessitate larger detectors to improve detection efficiency is of lower interest.

The last set of experiments was also performed with the HEU disk but with a few modifications. First, one or two steel plates were taped to the front of the NaI detector to provide attenuation. Second, the axial distance between detector and source was reduced from 38 cm to 8 cm (11 cm from the crystal), and finally only on-axis measurements were taken. These measurements simulated the attenuation that would be provided by steel pipes and equipment walls that normally stand between the detector and a holdup material deposit. The dimensions of the first steel plate were  $105.22 \text{ mm} \times 157.75 \text{ mm}$  ( $\pm 0.02 \text{ mm}$ ) with a thickness of  $0.86 \pm 0.04 \text{ mm}$ . The second plate was  $101.62 \text{ mm} \times 152.66 \text{ mm}$  ( $\pm 0.02 \text{ mm}$ ) and  $0.90 \pm 0.02 \text{ mm}$ . For visual reference, a photograph of the HEU attenuation experiment at 11 cm is shown in Fig. 2.

### 3. Monte Carlo transport models

Version five of the Monte Carlo code MCNP [17] was used to calculate the incident gamma-ray photon flux on the  $1'' \times 2''$  NaI detector crystal. For simplicity, in the MCNP simulation the isotopic compositions of the stainless steel plates were kept the same as the steel used to encase the detector and to encase the HEU source. The weight percent of each elemental isotope used in the steel alloy is listed in Table 4.

This composition of steel was taken directly from the MCNP detector model created by ORNL (note: due to rounding to 3 significant digits all listed weight percents sum up to 99.9%).

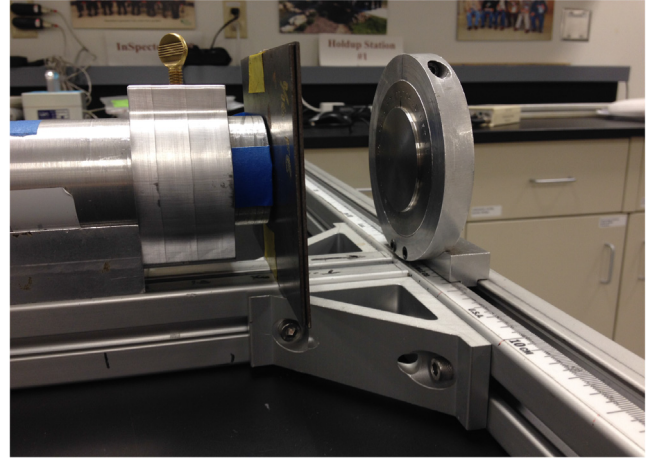


**Fig. 2.** The HEU disk attenuation experiment with two stainless steel plates attached to the detector (11 cm from the source).

**Table 4**  
Stainless steel alloy nuclide composition used in the MCNP simulations.

Nuclide	Weight %
Cr-50	0.800
Cr-52	16.2
Cr-53	0.200
Cr-54	0.400
Mn-55	2.00
Fe-54	4.20
Fe-56	64.8
Fe-57	1.50
Fe-58	0.200
Ni-58	6.60
Ni-60	2.50
Ni-61	0.100
Ni-62	0.300
Ni-64	0.100

The computational geometry specified for MCNP was simplified from the actual experimental geometric setups described in Section 2. Instead of including all details (i.e. objects) within the room, only the detector and all of its components and the source were simulated within a sphere of air. Only immediately adjacent objects like the table, the aluminum tee, and source holding apparatuses are likely to contribute to the collided fluence tally. There would be no contribution to the uncollided fluence tally as at least one Compton scatter with one of these objects would be required before the particle struck the detector. The detector collimator reduces the likelihood of these events further by reducing the detector face's solid angle. So, we assume that the secondary geometry (table, tee, etc.) would only make a negligible contribution to the Compton continuum portion of detector spectra and hence was excluded from the MCNP models.

With this simplified geometry, an F4 (average fluence) tally was taken in the detector crystal cell (filled with NaI, not void) by MCNP. MCNP calculates the fluence by summing the particle track lengths over the given cell volume for each discrete energy bin as specified by the user. In our case, 512 equal and discrete energy bins were chosen to match the energy range covered by the DRF, and to match the 512 channels observed in the measured spectra.

However, as the MCNP fluence is normalized per particle history, it can be normalized to the proper fluence magnitude as follows

$$\bar{\phi}(E) = \bar{\Phi}_V(E) \cdot A \gamma \left[ \frac{\text{photons}}{\text{cm}^2 \cdot \text{sec} \cdot \text{MeV}} \right]. \quad (3)$$



where  $A$  is the activity of the source in Becquerels (Bq) or decays/s, and  $\gamma$  is the yield in particles/decay. Multiplying the F4 tally (fluence) by the source activity and yield converts the tally to the approximate scalar flux effective over the volume of the detector crystal.

The detector response can be estimated by multiplying the DRF by the incident flux. However, Gardner's DRF model is generalized and also requires calculation of the detector's absolute efficiency, so it must be introduced into the formal definition. A differential pulse height spectrum (detector response),  $dN/dH$ , is defined as

$$\frac{dN}{dH} = \int R(H, E) S(E) dE \approx \sum_{i=1}^G R_G(H, E_i) \bar{\phi}(E_i) \epsilon_{abs}(E_i). \quad (4)$$

Again,  $R(H, E)$  is the differential probability that a photon of energy  $E$  leads to a pulse with amplitude within  $dH$  about  $H$ .  $S(E)dE$  is the differential number of incident photons with energy within  $dE$  about  $E$  [10]. Upon discretization of the formal definition appearing in Eq. (4) over energy groups  $i = 1, \dots, G$ , we obtain the practical expression on the right-hand side of Eq. (4) that is directly applicable to a multi-channelled detector. In this expression  $R_G(H, E_i)$  is Gardner's DRF, defined as the probability that a photon with energy within the energy range spanned by group  $i$  characterized by energy  $E_i$  leads to a discrete pulse with amplitude  $H$ , and  $\epsilon_{abs}(E_i)$  is the absolute efficiency.  $\bar{\phi}(E_i)$  is the volume-averaged flux over energy bin  $i$ . To fully determine a detector response using Gardner's model, the absolute efficiency must be modeled and calculated.

There are two main classes of detector efficiency, absolute efficiency and intrinsic efficiency. Knoll defines absolute efficiency as simply the ratio of the number of detector pulses recorded to the number of particles with energy  $E$  emitted from the source [10]. Absolute efficiency is dependent mainly on detector properties (cross sections) and the counting geometry (source to detector position). On the other hand, the intrinsic efficiency is the ratio of the number of detector pulses recorded to the number of radiation quanta incident on the detector [10]. The intrinsic efficiency is calculated within the DRF model, but the absolute efficiency is not. Therefore it is approximated as the energy deposited along the average path length through the detector crystal in MCNP simulation.

In other words, the absolute efficiency is the probability of particles with incident energy  $E$  interacting with the detector crystal (thereby creating a pulse at energy  $E$ ). This probability is proportional to the probability of interaction along a track length defined as

$$\epsilon_{abs}^j(E) \propto P_{interaction} = 1 - e^{-\mu_{tot}(E) \cdot s_j(E)}, \quad (5)$$

where  $\mu_{tot}(E)$  is the total NaI photon macroscopic cross section, and  $s_j(E)$  is the track length of particle history  $j$ . The MCNP routine called ptrac was used to record a large number of possible particle track lengths into and out of the detector crystal cell. The energy deposited in the crystal by particle interactions was compared to the total emitted by averaging over all of the track lengths to produce an average absolute efficiency  $\bar{\epsilon}_{abs}(E)$  as shown in Eq. (6)

$$\bar{\epsilon}_{abs}(E) = \frac{1}{N_t} \sum_{j=1}^{N_t} \epsilon_{abs}^j(E), \quad (6)$$

where  $N_t$  is the total number of track lengths recorded by ptrac. However, since Gardner's model typically underestimates the flat continuum under the response due to electron transport physics concerning channeling or possibly NaI impurities, the computed total response must be normalized to the experimental response [5]. In our work, the normalization factor (the ratio of the areas under each curve) necessary to raise the computed response to

the experimental profile was found to take a value in the range from 2 to 18 for the various configurations described in Section 4. This is in good agreement with the results in Ref. [5] where the experimental measurements were up to around an order of magnitude greater than the responses predicted by g03.

## 4. Validation

Overall, the detector responses simulated by Gardner's model predicted the highest intensity peak region of the experimental spectra fairly well but had some difficulty in the continuum and secondary peak regions. In the highest intensity peak region of the response, most of the computed spectrum lay within two experimental standard deviations of the experimental spectrum's centroid. As expected, the continuum and lower-energy peak regions of the experimental spectra were not as well predicted by the simulated response due to differences between the detector of interest and the original detectors and assumptions modeled by Gardner's DRF.

### 4.1. Cs-137 measurement

The first measurement was of a Cs-137 source. The Cs-137 source measurement was taken at a distance of 10 cm from the center of the detector face with the calibration source described in Table 1. The high source activity (4.13  $\mu$ Ci) allowed for a precise measurement with less than one percent uncertainty in the peak region in terms of counts (according to Poisson counting statistics), and it was counted for 4000 s. This source was used for validation and as one of the data points for the power law fit but not for the final energy calibration. The resulting measured spectrum for the Cs-137 source is compared to the responses computed with MCNP for the detector model including the lead collimator and the aluminum sheath (Fig. 3a) and excluding these two detector features (Fig. 3b).

In both plots of Fig. 3 the peak is underestimated, and in Fig. 3 (a) the backscatter peak (near 0.2 MeV) is slightly overestimated. However, the greatest difference lies in the area between the Compton edge and the peak, which will henceforth be referred to as the valley of the response. At first this effect was thought to be just a product of the model being unable to account for the collimator geometry, hence the numerical experiments reported in Fig. 3. In Ref. [18], a similar difference was observed in the valley region of the response for the employed 3"  $\times$  3" NaI detector. However, the sense of the difference between the computed and measured responses was reversed. For a bare NaI crystal simulation in MCNP for the flux calculation, the resulting response underestimated the valley. Simulating the detector aluminum sheath or the can raised the response profile, thus improving the agreement between the measured and computed responses [18].

In that manner, the same general effect is observed here. Removing the collimator and aluminum sheath from the MCNP geometry resulted in a response with a lower valley that is in better agreement with the measured response but is clearly less accurate physically. This leads us to conjecture that the collimator and can geometry are not the source of the shallow valley discrepancy. Instead it can likely be attributed to the imperfect tuning of the electron range multiplier factor, as a similar discrepancy was encountered in Ref. [5] while developing the electron range multiplier factor.

The similarity in discrepancies is not readily apparent due to a difference in how the computed spectrum was normalized to the measured response. Gardner and Sood chose to normalize to the peak channel only, whereas in this work, normalization to the area under the section of interest bounded by the normalization bounds

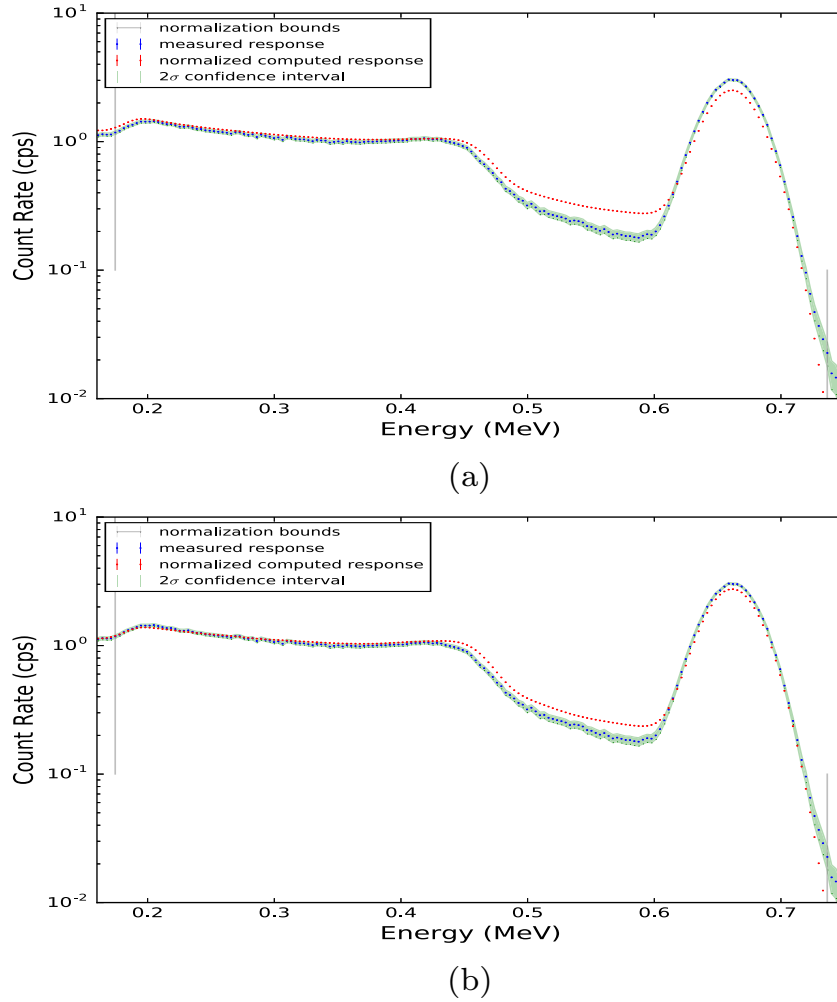


**Fig. 3.** Measured and computed responses for the Cs-137 calibration source at 10 cm (normalized over the energy range bounded by the vertical gray lines) with the MCNP model including the aluminum can and lead collimator (a) and excluding these two detector features (b).

was preferred because it avoids the need to choose one peak over another in multi-peaked spectra (possibly biasing the error). The normalization factor used to normalize the computed-to-measured ratio of the response spectrum is stated as

$$N_f = \frac{\sum_{i=n_{b1}}^{n_{b2}} R_i^m}{\sum_{i=n_{b1}}^{n_{b2}} R_i^c}, \quad (7)$$

where  $R_i^c$  is the computed count rate, and  $R_i^m$  is the measured count rate at channel  $i$ .  $n_{b1}$  and  $n_{b2}$  are the channel indices corresponding to the normalization bounds depicted in Fig. 3 by the vertical gray lines. Normalization bounds were chosen on a case-by-case basis, resulting in normalization factors in the range 2–18 cited in the last paragraph of Section 3. In this case the bounds were chosen to avoid bins artificially augmented by the rebinning process and unnecessary noise in channels above the full-energy peaks. Rebinning was accomplished via a standard algorithm by assuming the count rates within the old bins were uniformly distributed, and then collecting them into the new bins according to the fractions of the old bins determined by the uniform pdf. All contributions from the unphysical negative-energy bins created from the energy calibration were lumped into the first two bins by the rebinning algorithm. Therefore those two bins were not included in the normalization.

The main reason for choosing normalization bounds across sections of the detector response was to minimize the contribution to the response error from other parts of the spectrum. Again, the

other reason was to avoid biasing the error by choosing one peak to normalize to from multiple peaks in a spectrum. However, in this case normalizing to the peak channel revealed the true source of the valley problem as shown by the renormalized spectrum in Fig. 4a and Gardner's responses resulting from various electron range multipliers copied from Ref. [5] in Fig. 4b.

Now, as can be seen, the whole response spectrum is overestimated to the left of the peak in Fig. 4a. A similar effect is observed by a spectrum with an electron range factor that is too low in Gardner's results in Fig. 4b [5]. A range multiplier that is too high underestimates the continuum and the valley, and vice versa. Since the size of the detector and number of channels of the 1"×2" ORNL detector are different from Gardner's detector, it is not surprising that the value of the electron range multiplier may no longer be optimal in terms of agreement between the measured and computed responses. Furthermore, the pseudo-electron range multiplier (Eq. (2)) was fit for Gardner's detector by trial and error. For this reason, and the fact that the HEU spectrum of interest contains far less contribution from Compton scatter, the correction of the factor, important as it may be, is outside the scope of this work.

#### 4.2. Co-60 measurement

The next measurement concerned the Co-60 source described in Table 1 taped directly to the detector face. The low source activity (0.1927  $\mu$ Ci) required 1600 s for a reasonable number of counts

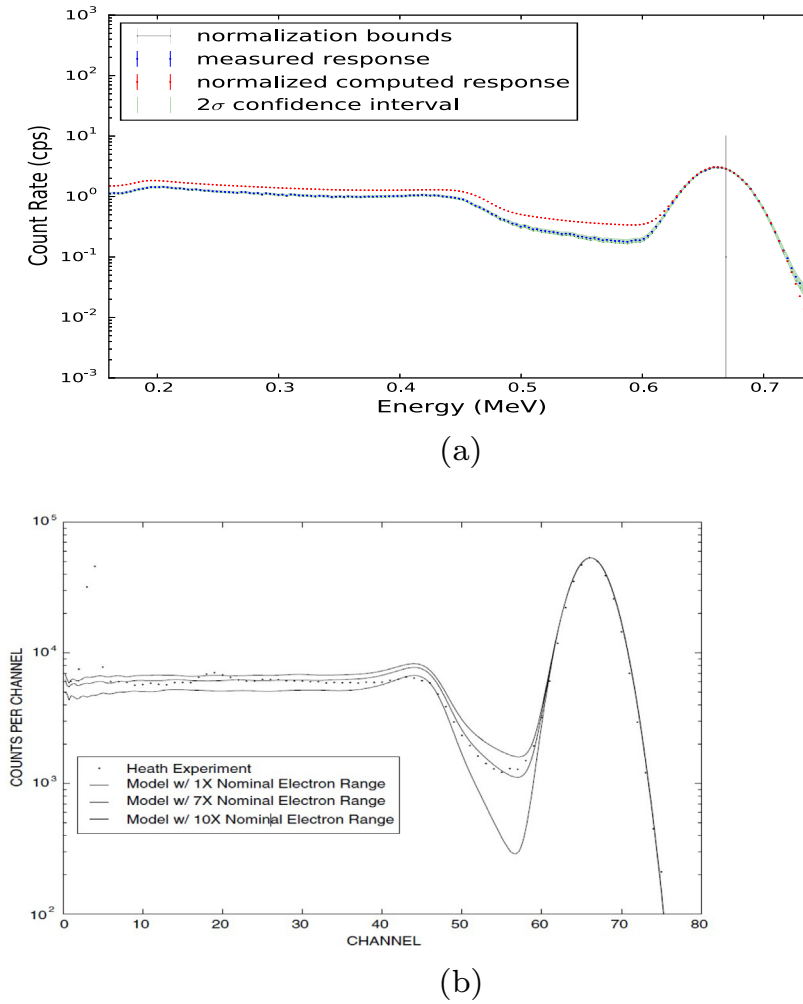


**Fig. 4.** (a) Measured and normalized computed responses for the Cs-137 calibration source at 10 cm (normalized to the peak). (b) Gardner's 3'' $\times$ 3'' NaI detector computed responses over a varying electron range multiplier compared with the measured response from the Heath benchmark; copied here from Ref. [5].

(400 counts, 5% Poisson uncertainty) even on the detector face, so no further measurements were taken with this source. However, this source was only used for the detector energy calibration and a simple baseline validation shown in Fig. 5 with normalization (a) over a span of the spectrum indicated by the vertical gray lines, and (b) to the highest peak indicated by a single vertical gray line. The energy calibration and its parameter uncertainties are discussed further in Section 5.2.

As expected, the measured spectrum shows some significant fluctuation in the  $\pm 2\sigma$  confidence interval due to the low number of counts (higher uncertainty). The bounded normalized computed response (from Fig. 5a) stays mostly well within the confidence interval of the measured response except at the backscatter peak around 0.2 MeV and the peaks are slightly underestimated. Also, the two Compton edges and most of the continuum are predicted fairly well.

However, the peak normalized spectrum (Fig. 5b) reveals that the same continuum overestimation observed in the Cs-137 case is also observed with Co-60 too. The overestimation may appear to be less significant than the Cs-137 case due to wider confidence bounds resulting from the lower fidelity of the measurement, but it is still apparent on closer inspection. The cause is most likely the same as the Cs-137 case, miscalibration of the electron range fit in the g03 code. Normalization bounds in this case too were chosen for the same reasons as the Cs case.

#### 4.3. HEU disk measurement set

The first set of HEU disk source measurements were performed in order to test the performance of the DRF model for off-axis geometry. All measurements were carried out at a distance of 41 cm on-axis ( $y$  direction) from the crystal face (38 cm from the detector front) and in set increments of 5 cm in the  $x$  direction. The central and first two positions ( $x = 0, 5, 10$  cm) used a 400 s background count, whereas the last two positions ( $x = 15, 20$  cm) used background count times equivalent to the measurement count times. All background count times were chosen based on propagation of the net count uncertainty. The normalized computed and measured responses are depicted in Fig. 6.

Unlike the Cs-137 and Co-60 cases, the HEU gamma radiation energies are too low to produce much of a Compton continuum, and any trace of such continuum is obscured by secondary peaks. Normalization bounds were chosen to include the high-yield U-235 full-energy peaks and exclude lead backscatter peaks (not simulated by the DRF model). The normalized computed spectrum modeled the measured spectrum fairly well (within two standard deviations of the experimental response) for the main full-energy peak at 186 keV and its shoulder peak at 205 keV with only a slight overestimation; however, the secondary peaks at 163 and 144 keV are underestimated. In general, scattering that occurs inside the detector crystal is accounted for by the DRF, but that which occurs

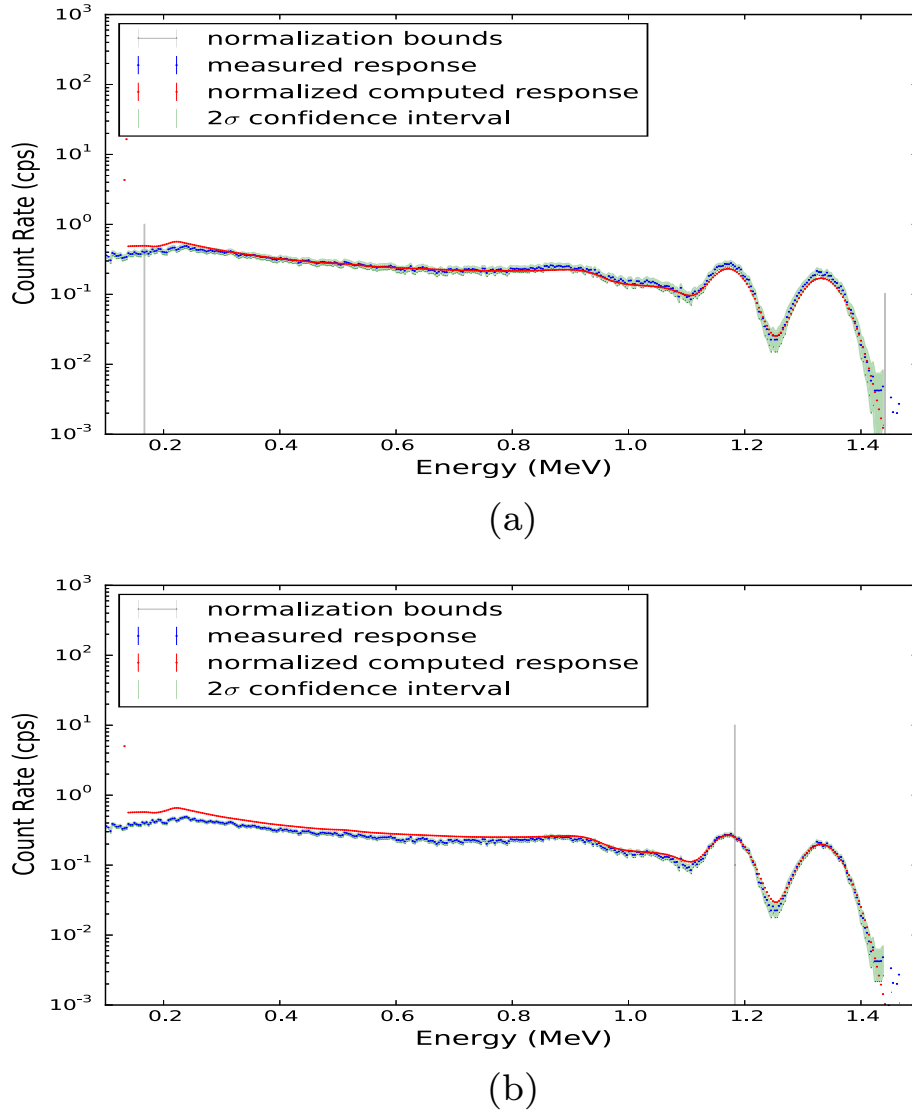


**Fig. 5.** (a) Measured and normalized computed responses for the Co-60 calibration source taped to the detector face using normalization across a range of channels (a) and normalized to the highest intensity peak (b).

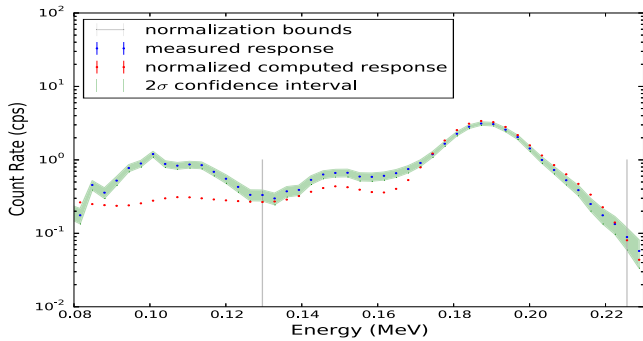


**Fig. 6.** Measured and normalized computed responses for the HEU disk at the central detection position ( $x = 0$  cm).

outside the crystal (e.g. in the lead shielding) is not [5]. It follows that absorption in the collimator created a significant decrease in the measured flux that is unaccounted for by the DRF. The lead cross sections listed in Ref. [19] support this conjecture by demonstrating an absorption cross section that is about six times larger

than the scattering cross section at 200 keV. The lead scattering cross section is  $0.1523 \text{ cm}^2/\text{g}$ , and the absorption cross section is  $0.8464 \text{ cm}^2/\text{g}$  at 200 keV.

In terms of mean free paths (mfp), the 3 cm of lead provided by the collimator is approximately 29 mfp in terms of absorption and only 3 mfp in terms of incoherent scattering. The collimator is now optically thick in terms of absorption but still thin in terms of a scatter. While scattering will still only reduce the flux of the highest full-energy peak of the spectrum, it would add to the flux of the lower energy peaks. This explains the overestimation of the high-energy peak balanced with the underestimation of the lower peak. The scattering also distorts the shape of the two overlapping peaks at 163 and 144 keV exhibiting only one peak at about 150 keV. Since simulation of the low-fidelity results with the peak DRFs summed and averaged in position and amplitude yielded better results than the two simulated separately, they were kept together for all subsequent simulations. The comparison of the low fidelity runs with the peaks separated and combined can be found Appendix A.1 of Ref. [14].

The lowest energy peaks below the normalization bounds were originally thought to be a set of four very low intensity peaks (109,



105, 93, and 90 keV, respectively). However, upon further investigation it was found that the backscatter peaks from the three main full-energy peaks could account better for the peaks appearing in the spectrum around 100 keV. Using the Compton scattering equation in terms of energy, it was calculated that the backscatter peaks from the lead shielding would be centered at 114, 108, and 95 keV for the full-energy peaks at 205, 186, and 150 keV, respectively. Therefore, the backscatter peaks are acknowledged but excluded from the normalization region in order to avoid skewing the other validation regions containing the full-energy peaks.

Three other factors could have also contributed to the underestimation of the two secondary peaks besides scattering in the collimator. Scattering within the table and aluminum tee that were not simulated in the MCNP fluence model, U-235 X-rays, and gamma rays emitted by the decay products of U-234, U-235, and U-238 (including Th-231) could also have made some contribution to the measured responses that was not included in the simulated response. It was assumed that scattered photons from the table and tee contribute negligibly due to shielding provided by the collimator. U-235 X-rays and gamma radiation from uranium daughter products were not simulated because they are of low energy and produce photons with low relative yields (refer to Ref. [16]).

The HEU disk source was measured at the first (5 cm off-axis) and second position (10 cm off-axis) for 500 and 750 s, respectively. The source at the third position (15 cm off-axis) and fourth position (20 cm off-axis) was counted for 1600 and 4800 s, respectively. The normalized computed and measured responses for these four cases are reported in Fig. 7.

The normalization interval was selected individually for each of these cases as described above. As expected, the entire count rate for all off-axis spectra is slightly decreased from the central position due to attenuation within the collimator and increased distance from the source. The lead backscatter peaks have also consolidated into a slightly different shape to accommodate a new set of scattering angles with the collimator. The computed response again overestimates the main full-energy peak and underestimates the secondary peaks due to the increased scatter from the collimator.

The underestimation worsens as the off-set distance increases and attenuation from the collimator increases. Beyond 15 cm, the secondary peak and the lead backscatter peaks become nearly indistinguishable from background radiation. The reason for this high background is that the experiment was designed to ensure only the visibility of the main 186 keV peak. The least-squares fit for the linear shifting process could not fit a Gaussian peak to the 150 keV peak for the  $x = 20$  cm position in Fig. 7d, so only a one-peak based shift was performed on this spectrum, and the normalization bounds were narrowed to enclose just the 186 keV peak.

#### 4.4. HEU disk attenuation measurement set

The second set of HEU disk measurements was conducted to test the DRF model's simulation of the response from attenuated sources. Each measurement was performed with the source centered on-axis at a distance of 11 cm from the crystal (only 8 cm from the detector's face). The first measurement was counted without any attenuators. The second and third cases involved affixing one and two stainless steel plates (thickness of approximately 0.9 mm each), respectively, to the face of the detector to approximate a pipe attenuating the radiation source. The count time was kept constant at 300 s for each of the three measurements, as the count rates were sufficiently high at this distance. The normalized computed and measured responses for these cases are reported in Fig. 8.

The same effects as observed before for the central position at 41 cm were observed for the unattenuated response: imbalance between the two full-energy peaks and missing the lead backscatter peak. However, the count rate is higher due to the closer proximity of the source. Naturally, the normalization bounds were kept the same as the inner ( $x \leq 15$  cm) axial HEU measurements. As stainless steel sheets are added to the face of the detector, a decrease in count rate across the entire spectrum is observed, but the shape of the spectrum remains largely unchanged with the addition of one and then two attenuators. The comparison between the measured and computed count rates is very similar to that of the off-axis cases; namely, the underestimation of the secondary peak worsens with increasing attenuation, except here

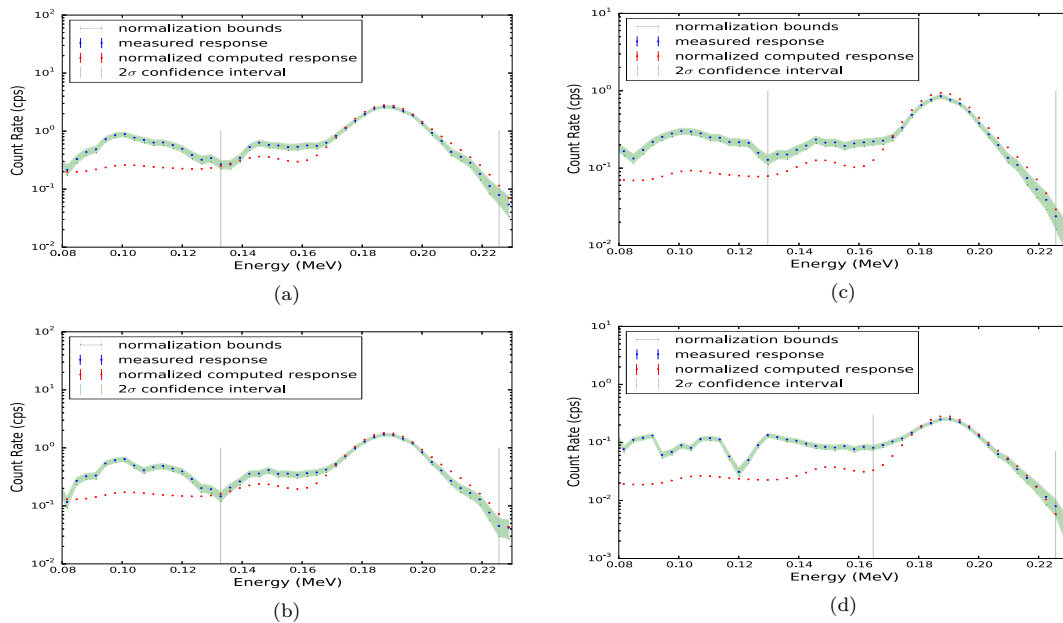


**Fig. 7.** Measured and normalized computed responses for the HEU disk source at  $y = 41$  cm and right of center at (a)  $x = 5$  cm, (b)  $x = 10$  cm, (c)  $x = 15$  cm, and (d)  $x = 20$  cm. The normalization interval, indicated by vertical gray lines, was selected for each case as explained in the text. Note left of center cases were very similar and are not shown here but can be found in Ref. [14].

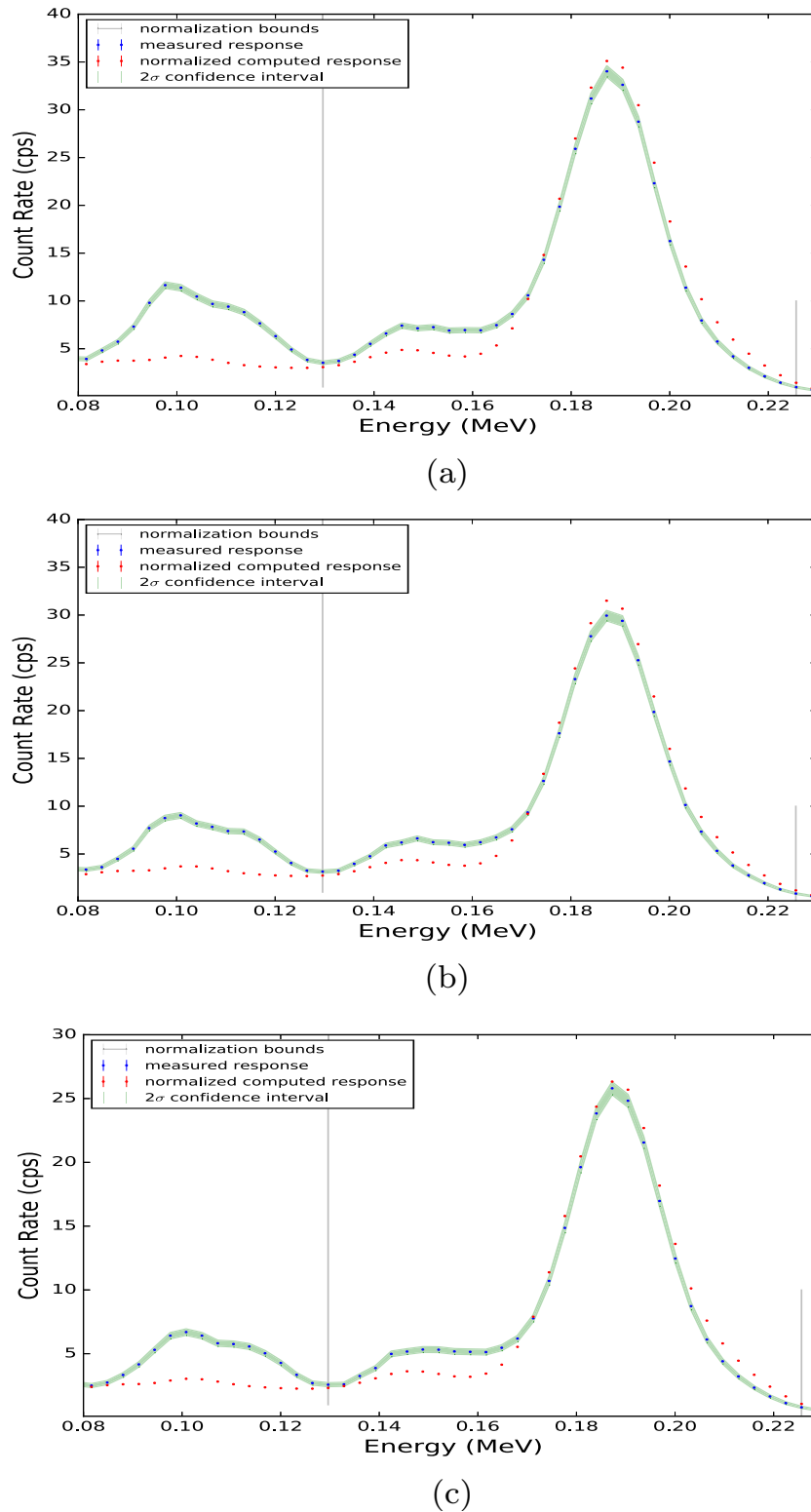


**Fig. 8.** Measured and normalized computed responses for the HEU disk source (a) without any, (b) with one, and (c) with two stainless steel sheets taped to the detector face.

the background shape does not change since the angle of incident radiation is constant.

### 5. Uncertainty quantification

The other major goal of this work is to quantify the uncertainties associated with the simulated responses. Validation reveals the accuracy of the model, whereas uncertainty quantification

yields the expected precision and possible bias of the simulated responses, providing a level of confidence in the computed results. Each step in calculating the detector responses has an associated uncertainty that has been calculated and compared to the experimental uncertainty where applicable.

Uncertainties that were easy to control (e.g. MCNP uncertainties are based on the number of histories run) were always reduced below the response peak channel uncertainty for each

measurement case. Fitting uncertainties were based on the number of data points available and the uncertainty in the data itself and therefore constrained to the quality of measurements performed. Even so, most of the fixed uncertainties tended to be smaller than the respective measurement's experimental Poisson uncertainty.

### 5.1. Monte Carlo-based sampling uncertainties

The MCNP fluence calculated by particle track length tallies in MCNP was separately accumulated into energy bins according to the energy structure of the DRF calculated by g03. MCNP calculates the relative uncertainty of each bin based on the number of particle track lengths that fall into that bin. Therefore, the number of total tallies was chosen in order to make the energy bin with the highest standard deviation attain the same uncertainty as the lowest experimental uncertainty for each measurement excluding the Am-241 seed peak region. This would guarantee that any sources of error greater than the experimental uncertainty could not be attributed to numerical uncertainty. The number of histories required was then computed as the reciprocal of the square root of the number of particle histories executed that represents the statistical uncertainty. In all cases, excluding Co-60, the number of histories required was on the order of billions to produce channel uncertainties above the X-ray range of under 1%. Similarly, in the Cs-137, Co-60, and HEU attenuation cases the highest computational uncertainties above 80 keV were ensured to be below the lowest uncertainty of the experimental results.

In certain cases of the HEU disk measurements at 41 cm, meeting the lowest experimental uncertainty objective for every tally energy bin was difficult to achieve in a reasonable amount of computational time. Certain MCNP modeling measures were taken to reduce computation times. First, the energy bins below 80 keV were excluded from the above requirement for two reasons. These bins had the highest computational uncertainty, and they were overshadowed by leftover noise from the background subtraction of the Am-241 seed peak in the measured spectrum anyway.

The other model modification involved reducing the source definition from an isotropic source to only producing particles within the solid angle calculated to actually strike the entire detector, not just its face. All particles were then weighted using a form of importance sampling called forcing to prevent biasing the fluence tally. The details of the derivation can be found in Ref. [14].

Since the table and room geometry are not simulated in the MCNP model anyway, it is a small approximation assuming that photons emitted outside of this angular range will not contribute to the detector response.

Rather than show all of the bin uncertainties for each case, the case with the highest uncertainty (HEU disk at  $x = 41$  cm,  $y = -20$  cm) excluding the Co-60 measurement will be given as an example. The fluence F4 tally is plotted with its uncertainty bounds in Fig. 9.

The bounds are fairly narrow for energies above 80 keV. Each spike in the fluence corresponds to a full-energy deposition by uncollided photons emerging from the HEU disk ranging from 105 keV to 205 keV; these correspond to the gamma lines of U-235. The largest relative standard deviation for  $E > 80$  keV was 2.44% at 195 keV. This is well below the lowest relative standard deviation of the HEU disk measurements at 41 cm, which was 2.72%. As can be seen, the confidence range between the 186 keV peak and the maximum energy peak at 205 keV is wider than anywhere else above 80 keV. Even the bins  $E < 80$  keV did not exceed 5% relative standard deviations.

The DRF itself contains a Monte Carlo calculation that fully calculates the probabilities of a count in each channel based on con-

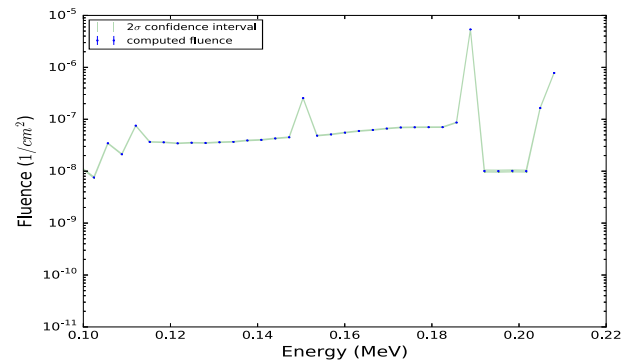


Fig. 9. MCNP computed fluence and two sigma confidence interval.

tributions from all other channels using the fit parameters. Once again, the number of particle histories controls the relative uncertainty of the DRF, and the same threshold of the lowest experimental uncertainty for each case was selected for the highest DRF channel uncertainty. The number of particle histories required was much less than that of the flux calculations and only on the order of hundreds of thousands for all DRF Monte Carlo calculations.

Again, it is not feasible to show every uncertainty for each measurement, so only the highest uncertainty case (excluding Co-60) is shown. As expected, this case is the HEU disk at 41 cm for the off-axis experiments. Furthermore, six DRFs (one for each incident photon energy) are summed together to produce the total DRF, so the peak DRF with the highest uncertainty (105 keV peak) was chosen as the representative example. Because g03 did not have a second axis distance variable, only one total DRF was used for the off-axis HEU disk experiments. Now, since the full DRF matrix is a two-dimensional object, it will be easier to display and interpret the uncertainty bounded along the peak channel DRF vector, as displayed in Fig. 10.

The highest probability density channel contributions for channel 33 are the immediate channels above that channel as expected from the spread of Gaussian uncertainty. However, the peak of the densities is actually about five to six channels over channel 33, which might explain the need to shift the computed spectra about the same number of channels. Channels above the spread have no contribution (density = zero), and the channels below are fairly constant. When the entire DRF is multiplied by the flux, the entire row of densities for each channel is multiplied by the flux vector and summed, so naturally the uncertainty is constant for each channel. The relative standard deviation for this channel was 0.420% and well under the 2.72% experimental uncertainty. Each channel row in the DRF possesses a similar density curve, so the

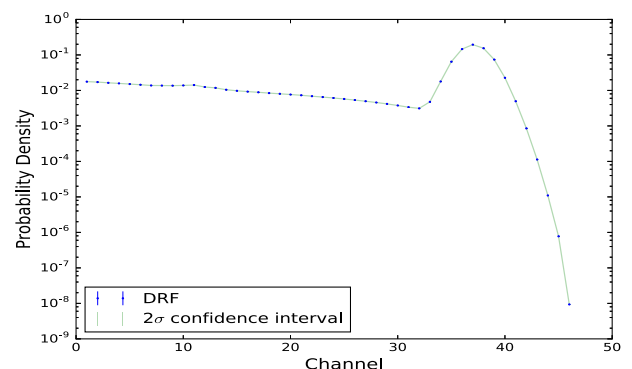
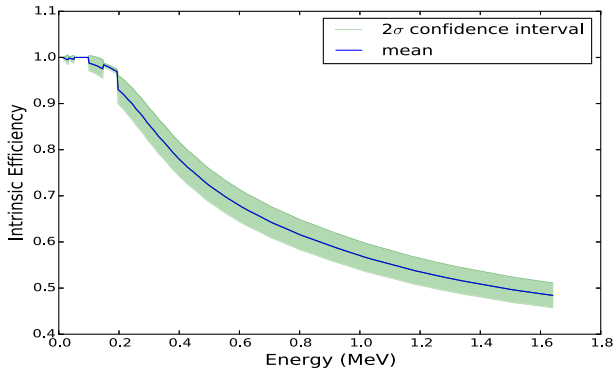


Fig. 10. HEU disk at 41 cm with DRF probability densities for the 105 keV peak at channel 33 and the two sigma confidence interval.



**Fig. 11.** Absolute efficiency of the NaI ORNL field holdup detector and two standard deviation confidence interval.

highest flux channel will produce the highest response automatically. The highest relative standard deviation of all the DRF channels occurred in the last channel (512) and was only 1.80%.

The total absolute efficiency calculation was carried out through calculation with an XCOM NaI cross section and particle track lengths through the crystal volume in MCNP as described by Eq. (6). The number of histories was increased accordingly until the proper number of path lengths was acquired to reduce the highest relative standard deviation to approximately that of the lowest experimental uncertainties. The highest uncertainty case is observed for the HEU disk at 41 cm. The resulting probability density curve with a two sigma confidence interval is shown in Fig. 11.

This curve is essentially the probability of an interaction of a photon with energy  $E$ , occurring within the crystal, so low energies are almost certain to be absorbed and higher energies are more likely to escape. The relative uncertainty is fairly small at low energies, but grows as energy increases. The relative standard deviation was 2.78% at the highest energy, which was close to the lowest experimental relative uncertainty of 2.72%. At 0.2 MeV or less where the majority of the HEU spectrum lies the relative uncertainty is much lower and well below 1%. The discontinuities observed just below 0.2 MeV are a result of the higher number of particles tallied for the 186, 163, and 144 keV source emission photons than the distributed Compton scattered photons. The lower energy discontinuities near 30 keV correspond to the K-edge discontinuities in the NaI cross section. The higher constant uncertainty at energies greater than 0.2 MeV is due to lack of data, as 205 keV is the highest energy photon tallied. The efficiency and its uncertainty are merely extrapolated from that point on.

## 5.2. Parameter uncertainties

The first set of parameters is associated with both the measured and computed results: the energy calibration. The energy calibration is a polynomial that converts channel data to energy data based off of the nonlinear scintillation behavior of NaI detectors. This is a necessary piece of data for interpreting physical measurements and a required conversion for the empirical power law of the DRF. The energy polynomial is given by

$$E = \alpha_2 h^2 + \alpha_1 h + \alpha_0, \quad (8)$$

where  $h$  is the channel index,  $E$  is photon energy, and  $\alpha_0$ ,  $\alpha_1$ , and  $\alpha_2$  are the polynomial fitting parameters. The energy calibration parameters were found by a least-squares fit of measurements of known sources with known energies. Three sources were used to determine the energy calibration polynomial: the Am-241 seed source, and the Cs-137 and Co-60 sources detailed in Table 1. Each

**Table 5**

Channel means and associated standard deviations (STD) of the Gaussian fits for the energy calibration.

Source	Pk. No.	Mean Chan., $\bar{x}$	STD, $\sigma^x$	Rel. STD, $\sigma_{rel}^x$ (%)	Red. Chi-Square, $\chi_v^2$
Am-241	1	20.92	2.767E-3	1.323E-2	0.8973
Cs-137	1	195.79	1.804E-2	9.212E-3	2.569
Co-60	1	341.64	0.2214	6.479E-2	1.059
Co-60	2	386.38	0.1761	4.557E-2	0.7260

channel mean for the energy calibration was found by taking the peak section of the measured responses for each source and fitting it according to a simple Gaussian plus linear background empirical model. The linear Gaussian model is given by

$$G_y = \frac{B}{\sqrt{2\pi}\sigma_T} e^{-\frac{1}{2}(\frac{h-\bar{h}}{\sigma_T})^2} + a_1(h - \bar{h}) + a_0, \quad (9)$$

where  $h$  is again the detector channel and  $G_y$  is the resulting point in the Gaussian curve.  $B$  is the normalization constant, and  $\sigma_T$  is the standard deviation of the Gaussian. Finally,  $\bar{h}$  is the mean of the Gaussian, and  $a_0$  and  $a_1$  form the linear background term. The Gaussian channel means and parameter standard deviations for the 1"×2" NaI detector employed in this work are shown in Table 5.

Each least-squares fit was performed by a nonlinear least-squares algorithm in MATLAB called lsqnonlin. The standard deviation was found through the simple Frequentist methods described in Section 1.2 from the parameter covariance matrix. Classical Frequentist methods were used in lieu of Bayesian for all Gaussian peak fitting except for the power law measurements because there were usually a large number of data points in each peak. Also, Frequentist calculations require shorter execution time than DRAM (about a factor of 100 times less). The algorithm had no trouble fitting these peaks, as each relative standard deviation of the mean channel is well under 1%. Co-60, as expected, had the highest uncertainty because it had the lowest source strength and a low count time (low fidelity measurement). However, all peaks were well approximated by the model producing reduced chi-squares well under 3.

A simple polynomial fit was used for the detector energy calibration. Overall, the calibration performed well, as each channel mean converted to energy was found to be within 2 keV (1% relative error) from its true value for all peaks that were not convolved with another peak (e.g. the 150 keV convolved HEU peak). This is acceptable because the same energy calibration is used for both computed spectra and measured spectra, so any additional error would offset both spectra by the same amount. In other words, the energy calibration error is independent of the other DRF modeling errors.

The next set of parameters involves the power law (Eq. (1)) of the DRF model itself. g03 not only uses Monte Carlo simulation to calculate DRFs, it also requires an empirically fit power law based on Gaussian spread data from the detector of interest.

Again, linear Gaussian (Eq. (9)) least-squares fits of several sources were required to obtain mean Gaussian standard deviations for the power law. Five sources were used: Am-241 (seed source), Ba-133, Cs-137 (same as in Table 1), Mn-54, and Na-22. Since Ba-133 has two full-energy peaks, a total of six full-energy peaks were fit.

Source geometry and activity were not required for the power law fit. However, each peak was counted until 10,000 counts were registered in the peak channel to keep the experimental uncertainty close to one percent in the peak region. Some weak sources needed multiple measurements added together to meet 10,000 counts due to the MCA timer limit. Furthermore, there should be



**Table 6**

Channel means and associated standard deviations of the Gaussian fits for the power law.

Source	Pk. No.	Energy (MeV)	Gauss. STD, $\sigma_T$	STD, $\sigma^{\sigma_T}$	Rel. STD, $\sigma^{\sigma_T}_{rel}$ (%)	$\chi^2_\nu$
Am-241	1	5.954E–2	4.454E–3	2.128E–5	0.4778	0.9191
Ba-133	1	8.100E–2	4.879E–3	4.478E–4	9.177	56.51
Ba-133	2	3.560E–1	1.499E–2	2.106E–4	1.405	13.09
Cs-137	1	6.617E–1	2.137E–2	7.599E–5	0.3556	2.295
Mn-54	1	8.348E–1	2.468E–2	8.469E–5	0.3432	1.011
Na-22	1	1.275	3.207E–2	8.001E–5	0.2495	1.611

**Table 7**

Linear correlation coefficients for the 81 keV Ba-133 linear Gaussian model fit.

Parameter	$\sigma_T$	$\bar{x}$	$B$	$a_0$	$a_1$
$\sigma_T$	1	–0.9594	0.9901	–0.9838	0.9737
$\bar{x}$	–0.9594	1	–0.9727	0.9664	–0.9801
$B$	0.9901	–0.9727	1	–0.9978	0.9922
$a_0$	–0.9838	0.9664	–0.9978	1	–0.9936
$a_1$	0.9737	–0.9801	0.9922	–0.9936	1

no added uncertainty in the measurements because the spectra were checked for gain drift and performed immediately after one another. The mean Gaussian standard deviations ( $\sigma_T(E_i)$ ) and their uncertainties are compiled in Table 6.

Some of the peaks involved in the Gaussian fits for the power law spread data were sparse in data points, so DRAM was used to optimize the Gaussian spread parameter means ( $\sigma_T$ ) and determine their respective standard deviations ( $\sigma^{\sigma_T}$ ). Most of the fits had low uncertainty and good chi-square values under 3. The first Ba-133 peak had substantial background signal interference from the Am-241 seed source peak, and the 81 keV Ba-133 peak also had fewer points for fitting the corresponding linear Gaussian curve which resulted in the highest uncertainty and a reduced chi-square well over 10. The second Ba-133 peak was also over 1% in relative uncertainty and had a reduced chi-square over 10. This was probably due to some interference with a third lower intensity peak at 300 keV obscuring the left tail of the Gaussian.

To further investigate the large chi-square values for the Ba-133 peak Gaussian fits, we checked if the linear correlation coefficients of the model could reveal those model parameters with low contributions to the fit solution. If the correlation coefficients of a parameter are all under about 0.2, then that parameter shares no linear relationship with any of the other parameters. Sometimes, removing such parameters from the model can improve the fit. An example of this model is provided using the worst fit case to check for model weaknesses. The linear correlation coefficient matrix for the first Ba-133 peak (81 keV) is listed in Table 7.

All of the coefficients are highly correlated ( $> 0.9$ ), so there are no weak parameters. This does not mean that the model cannot be improved, just no terms should be removed. Maybe a few terms could be added to account for the nonlinear tail of the 60 keV Am-241 seed peak; however, a more practical alternative was found by weighting the power law fit by the experimental Poisson uncertainties at each point. This was more expedient than the other alternative of using a convolved peak model to improve the fit, which may not have lowered the parameter uncertainties significantly since the Ba-133 source had a low activity (similar to the Co-60 source activity).

This alternative was developed in response to the higher uncertainty in the Ba-133 peaks and the distrust in the Am-241 seed peak due to lack of exact knowledge of the seed's position relative to the center of the crystal. Originally, only three sources were used to calibrate the DRF power law, but results showed some error in the peak widths of some of the validation measurements. To resolve this issue, the power law fit was thought to be improved

with extra measurements at energies between the three original points. However, rather than throw out less-than-ideal data points for the power law, the least-squares fit was simply adjusted to weight each data point by its uncertainty. Instead of purely minimizing the sum of squares (classical least squares), the following weighted sum of squares was minimized.

$$WSS_q = \sum_{i=1}^n \left( \frac{Y_i - f(x_i, p_j)}{\sigma(x_i)} \right)^2. \quad (10)$$

Here,  $n$  is the total number of data points.  $Y_i$  is the measured result at data point  $i$ , and  $f(x_i, p_j)$  is the value of the function being fit to the data at  $i$ .  $p_j$  are the parameters, and  $\sigma(x_i)$  is the standard deviation of  $Y_i$  used as a weight. In this case the function fit is the power law, Eq. (1), and  $Y$  is  $\sigma_T(E)$ .

The rest of the least-squares and uncertainty calculations remained the same. The resulting parameter means and standard deviations of the weighted power law fit are provided in Table 8.

There were several data points for the power law, and it was uncertain if the weighted sum of squares would behave well with the Bayesian code. So, the classical Frequentist values were used in the DRF calculations for expedience. The Bayesian code was tested later and gave comparable results which are given in Appendix A.2 of Ref. [14] but skipped here. The parameter values are on the order of Gardner and Heath's (Ref. [5]) power law coefficients, and the relative standard deviations are under 1%. The power law is fairly overfit ( $1E-6$ ), but that is somewhat expected as several extra measurements were taken when the three-point fit proved insufficient. Also, the model is quite simple, so parameter reduction and model simplification are not viable options in this case.

The final process requiring uncertainty quantification is the linear energy shift required to align the computed and measured spectra. An unfortunate artifact of g03 tends to offset the entire spectrum by several channels to the right. A program called gshift (courtesy of Gardner's group) corrects this issue by linearly interpolating between the channels and "gain" shifting [9] the pulse height spectrum to the desired channels according to

$$x_{chan} = C \cdot E_p + D, \quad (11)$$

$$E_p = E \cdot f(E), \quad (12)$$

where  $x_{chan}$  is the channel number, and  $C$  is a normalization constant.  $D$  is the number of background channels, and  $E_p$  is the energy of the original pulse-height spectrum. Finally,  $E$  is the true energy of the gamma-ray (or desired energy to shift the peak to), and  $f(E)$  is

**Table 8**

Power law parameter values and standard deviations.

Parameter	Value	Standard Deviation, $\sigma$	Relative STD, $\sigma_{rel}$ (%)	$\chi^2_\nu$
a	0.027608	1.684E–4	0.6100	8.500E–6
b	0.644237	5.719E–3	0.8877	

**Table 9**

Computed spectrum channel means and associated standard deviations of the Gaussian fits for the energy shift.

Source	Pk. No.	Mean Chan., $\bar{x}$	Stand. Dev., $\sigma^*$	Rel. STD, $\sigma^*_{rel}$ (%)
Cs-137	1	204.67	9.799E–3	4.788E–3
Co-60	1	354.68	1.310E–2	3.692E–3
Co-60	2	397.71	7.363E–3	1.851E–3
HEU disk	1	52.22	1.610E–2	3.084E–2
HEU disk	2	64.51	1.093E–2	1.695E–2

**Table 10**

Experimental net spectrum channel means and associated standard deviations of the Gaussian fits for the energy shift.

Source	Pk. No.	Mean Chan., $\bar{x}$	Stand. Dev., $\sigma^*$	Rel. STD, $\sigma^*_{rel}$ (%)	$\chi^2_\nu$
Cs-137	1	195.79	1.804E–2	9.212E–3	2.569
Co-60	1	341.64	0.2214	6.479E–2	1.059
Co-60	2	386.38	0.1761	4.557E–2	0.7260
HEU disk	1	46.90	0.8512	1.815	0.5671
HEU disk	2	58.30	3.464E–2	5.942E–2	8.139E–2

the functional relationship of the ratio:  $Ep/E$ .  $C$  and  $D$  are adjusted accordingly to shift the peak(s) to the desired location, while  $f(E)$  is chosen by the user. Either  $f(E)$  is based off of the natural NaI non-linearity (for two or more peaks) or directly proportional (for one peak).

In order to determine the linear shift required, the mean peak channels of both the measured and computed spectra had to be found. The means were found in the same manner as those for the energy calibration fit, by fitting the spectral peaks to the linear Gaussian model (Eq. (9)). The Gaussian peak channel means and the associated uncertainties for the computed spectra are given in Table 9, and those of the measured spectra in Table 10.

All of the computational channel relative standard deviations were well under 1% (lowest Poisson uncertainty estimated from highest peak channels), but not all of the net (background subtracted) experimental ones were. However, the experimental channel uncertainties that exceeded 1% occurred only in the lower intensity 150 keV peak of the 41 cm HEU disk measurements. Furthermore, those uncertainties were expected to be high as the uncertainty of the these measurements was 2.72%. Reduced chi-square values are shown for the experimental responses to verify goodness of fit of the experimental data. Most of the values are fairly close to one.

All of the computational peak fits naturally had much lower uncertainties than the experimental peak fits, as the underlying DRF models Gaussian response peaks. Some of the 150 keV experimental peaks of the far off-axis HEU disk measurements were not well developed and could not be fit. In these cases, the shifting program employed the single-peak-shift algorithm instead of using only the main 186 keV peak channel means to shift the computed spectrum in alignment with the measured response.

## 6. Conclusion

We conducted three major sets of response measurements: on-axis detection of calibration sources, off-axis measurements with a HEU disk, and the HEU disk with steel plate attenuation between

the source and detector. In terms of the calibration source spectra with one or two peaks and a Compton continuum, the computed spectrum predicted the peak well within two standard deviations of the experimental count rate, but overestimated the continuum and valley between the peak and Compton edge. This discrepancy likely resulted from miscalibration of the electron range multiplier (Eq. (2)) used originally for an uncollimated 3"  $\times$  3" detector, as the same effect was observed in the validation exercise reported in Ref. [5] when the multiplier was set too low.

However, this effect did not appear in the two experimental campaigns involving the HEU disk, as the highest energy peak observed was of too low an energy to create an observable Compton continuum. The model reproduced the main peak (186 keV) and its shoulder peak (205 keV) well, again within two standard deviations of the measured count rate, but underestimated the convolved peak at (150 keV) and did not reproduce the lead backscatter peak near 100 keV. This was most likely due to scattering in the lead collimator that was unaccounted for by the DRF model, as the model currently only reproduces the effects of scattering within the detector crystal. However, local geometry (such as the table, detector electronics, etc.) and uranium daughter products, that were not included in the simulation, may have also contributed to response discrepancies.

Finally, uncertainty quantification of the model was conducted on every calculated quantity from the flux calculation in MCNP to the Gaussian peak fits for the spectral shifting program. Where the uncertainty was controllable by the number of particle histories chosen in Monte Carlo simulations, it was reduced below the lowest measured uncertainty. Where it was constrained to the accuracy of the model for least-squares fitting, the reduced chi-square test was performed to check for goodness of fit.

Of the approximately fifty fits conducted in this study only two mediocre least-squares fits were encountered: the energy calibration and the Ba-133 Gaussian peak fits used for the power law fit. The effects of the energy calibration were found to be inconsequential to the validation results. The Ba-133 peaks effects on the power law were minimized through a weighted least-squares

sum weighted by the uncertainties in the Gaussian peak uncertainties ( $\sigma^2$ ). Future research will incorporate an accurate DRF model for the general inverse problem approach whose efficient solution uses the adjoint flux, and where the adjoint source is the DRF. Perhaps Gardner's DRF matrix could be filtered for the peak DRF and used in such research.

## Acknowledgments

The first two authors of this work would like to acknowledge support from the U.S. Department of Energy's Nuclear Energy University Program under contract 127981. The authors would also like to acknowledge Steven L. Cleveland at Oak Ridge National Laboratory for his assistance with the experimental data collection presented in this paper.

## References

- [1] D. Reilly, N. Ensslin, H. Smith Jr., et al., Passive Nondestructive Assay of Nuclear Materials, Los Alamos National Laboratories, 1991, March. [Online]. Available: <http://www.lanl.gov/orgs/n/n1/panda/>. [Accessed 30 August 2012].
- [2] H. Dou, R. Li, J. Xu, et al., Modeling detector response function of alpha particles for neutron depth profiling, *Sci. China Technol. Sci.* 57 (1) (2014) 35–38.
- [3] K. Arakelyan, A. Daryan, L. Kozliner, et al., Design and response function of NaI detectors of Aragats complex installation, *Nucl. Instrum. Methods Phys. Res., Sect. A* 763 (2014) 308–313.
- [4] M.S. Tohme, J. Qi, Iterative image reconstruction for positron emission tomography based on a detector response function estimated from point source measurements, *Phys. Med. Biol.* 54 (12) (2009) 3709–3725.
- [5] R.P. Gardner, A. Sood, A Monte Carlo simulation approach for generating NaI detector response functions (DRFs) that accounts for non-linearity and variable flat continua, *Nucl. Instrum. Methods Phys. Res. B* 213 (2004) 87–99.
- [6] R.L. Heath, *Scintillation Spectrometry Gamma-Ray Spectrum Catalogue*, Idaho National Laboratory, Idaho Falls, ID, 1964.
- [7] M.J. Berger, S.M. Seltzer, Response functions for sodium iodide scintillation detection, *Nucl. Instrum. Methods* 104 (1972) 317–332.
- [8] D.E. Peplow, Sodium iodide detector response functions using simplified Monte Carlo simulation and principal components, *Nucl. Geophys.* 8 (3) (1994) 243–259.
- [9] J. Wang, Z. Wang, J. Peeples, H. Yu, R.P. Gardner, Development of a simple detector response function generation program: the CEARDRFs code, *Appl. Radiat. Isot.* 70 (2012) 1166–1174.
- [10] G.F. Knoll, *Radiation Detection and Measurement*, John Wiley & Sons, Hoboken, NJ, 2000.
- [11] W.L. Dunn, J.K. Shultis, *Exploring Monte Carlo Methods*, Academic Press, Burlington, MA, 2012.
- [12] R.C. Smith, *Uncertainty Quantification*, Society for Industrial and Applied Mathematics, Philadelphia, 2014.
- [13] Nuclear Safeguards and Non-Destructive Assay, Holdup Measurement System 4 (HMS4) Systems for Safeguards Measurements, ORTEC, 2014. [Online]. Available: <http://ortec-online.com/Products-Solutions/Applications-Software-Waste-and-SFGDS.aspx>. [Accessed 14 June 2015].
- [14] N. Nelson, Validation and Uncertainty Quantification of a 1"×2" NaI Collimated Detector Using Detector Response Functions Created by g03 (MS thesis), North Carolina State University, 2014.
- [15] Eckert & Ziegler Isotope Products, Eckert & Ziegler Reference & Calibration Sources: Product Information, Valencia, CA, 2007.
- [16] National Nuclear Data Center, Nudat2.6: Decay Radiation Search, Brookhaven National Laboratory, 2013. [Online]. Available: <http://www.nndc.bnl.gov/nudat2/indxdec.jsp>. [Accessed 14 June 2015].
- [17] X-5 Monte Carlo Team, MCNP – Version 5, vol. I: Overview and Theory, LA-UR-03-1987, 2003.
- [18] A. Sood, A New Monte Carlo Assisted Approach to Detector Response Functions (Ph.D. thesis), North Carolina State University, 2000.
- [19] M.J. Berger, J.H. Hubbell, S.M. Seltzer, J. Chang, J.S. Coursey, R. Sukumar, D.S. Zucker, K. Olsen, XCOM: Photon Cross Sections Database, National Institute of Standards and Technology, 9 December 2011. [Online]. Available: <http://www.nist.gov/pml/data/xcom/>. [Accessed 15 July 2014].